Mapping lateral variations in upper mantle attenuation by stacking *P* and *PP* spectra

Linda M. Warren and Peter M. Shearer

Cecil H. and Ida M. Green Institute of Geophysics and Planetary Physics, Scripps Institution of Oceanography, University of California, San Diego, La Jolla, California, USA

Received 12 September 2001; revised 10 April 2002; accepted 7 May 2002; published 12 December 2002.

[1] We study the lateral variations in *P* wave attenuation in the upper mantle at frequencies between 0.16 and 0.86 Hz by analyzing the spectra from >18,000 *P* and >14,000 *PP* arrivals. We select seismograms from shallow earthquakes at epicentral distances of 40°–80° for *P* waves and 80°–160° for *PP* waves. Each spectrum is the product of source, receiver, and propagation response functions as well as local source- and receiver-side effects. We correct each spectrum for average source and attenuation models. Since there are multiple receivers for each source and multiple sources for each receiver, we can approximate the source- and receiver-side terms by stacking the appropriate *P* log spectra. The resulting source-specific response functions include any remaining source spectrum and near-source *Q* structure; the receiver stacks include the site response and near-receiver *Q* structure. We correct the *PP* log spectra for the appropriate source- and receiver-side stacks. Since attenuation in the lower mantle is small, the residual log spectrum approximates attenuation in the upper mantle near the *PP* bounce point and is used to estimate $\delta\overline{t^*}$. We constrain the anomalies to the top 220 km of the mantle, as suggested by previous *Q* studies, and translate the $\delta\overline{t^*}$ measurements to variations in $1000/Q_\alpha$. The patterns of more and less attenuating regions generally correlate with previously published shear attenuation models and surface tectonics. Continents are usually less attenuating than the global average, whereas oceanic regions tend to be more attenuating. There are interesting exceptions to this tectonic pattern, such as an attenuating region beneath southern Africa. *INDEX TERMS:* 7203 Seismology: Body wave propagation; 7207 Seismology: Core and mantle; 7218 Seismology: Lithosphere and upper mantle; 7299 Seismology: General or miscellaneous; 8124 Tectonophysics: Earth's interior—composition and state (old 8105); *KEYWORDS:* attenuation, body waves, upper mantle, *Q*, lateral variations, global

Citation: Warren, L. M., and P. M. Shearer, Mapping lateral variations in upper mantle attenuation by stacking *P* and *PP* spectra, *J. Geophys. Res.*, *107*(B12), 2342, doi:10.1029/2001JB001195, 2002.

1. Introduction

[2] Both the elastic and anelastic structure of Earth are important for determining its composition, temperature, and dynamics. Together they can better constrain whether the spatial variations we observe are caused by thermal or compositional heterogeneities. The elastic structure of Earth is relatively well resolved: tomographic images of velocity perturbations [e.g., *van der Hilst et al.*, 1997; *Grand et al.*, 1997; *Masters et al.*, 1996] clearly show features such as slabs sinking into the lower mantle, slow regions around hot spots, and a low-velocity zone at the core-mantle boundary that help us infer the dynamics of the mantle. Measurements of the anelastic structure of Earth are more strongly influenced by focusing, scattering, and other effects that make reliable measurements more difficult, and only in the last few years have researchers begun mapping both the even and odd degrees of structure in the lateral variations of the quality factor *Q* on a global scale [e.g., *Romanowicz*, 1995; *Bhattacharyya et al.*, 1996; *Selby and Woodhouse*, 2000; *Billien et al.*, 2000].

[3] Free oscillation and surface wave data have allowed researchers to model the depth dependence of attenuation. These studies [e.g., *Dziewonski and Anderson*, 1981; *Widmer et al.*, 1991; *Durek and Ekström*, 1996] generally divided the mantle into distinct layers and solved for average *Q* values for each layer. An important result from these studies is that, on average, the most attenuating part of the mantle is the top layer. Most attenuation occurs in a relatively thin layer on the top of the mantle whereas attenuation is much less at greater depths. The lowermost mantle near the core-mantle boundary may also be an area of increased attenuation.

[4] Regional studies [e.g., *Der et al.*, 1982] have revealed large lateral variations in attenuation. They have also shown that how much seismic waves are attenuated in a given region often reflects its tectonic history. For example, the most attenuating regions tend to be areas with high temperatures and possibly partial melt, such as mid-ocean ridges

0148-0227/02/2001JB001195$09.00

[e.g., *Sheehan and Solomon*, 1992; *Ding and Grand*, 1993], back-arc basins [e.g., *Flanagan and Wiens*, 1990] and hot spots, whereas the least attenuating regions tend to be cold, stable areas, such as continental interiors [e.g., *Der et al.*, 1986; *Mitchell*, 1995]. These trends, along with the knowledge that most attenuation occurs at relatively shallow depths, means that the differences in attenuation seen for different paths through Earth can be mainly attributed to the tectonic settings surrounding the earthquakes and stations rather than the deeper parts of their paths.

[5] Improved global coverage by seismic networks has allowed studies of lateral variations to be extended to a global scale. Most global studies have used free oscillations and surface waves to map lateral variations in shear wave attenuation. In contrast, this study uses body waves to map lateral variations in compressional attenuation. We compute the spectra for relatively high frequency *P* and *PP* arrivals and measure how attenuated each arrival is from its spectral decay with frequency. Next, we use a stacking technique to map the observed attenuation to the upper mantle beneath the sources, receivers, and *PP* bounce points. While the source- and receiver-side terms are affected by factors such as the source spectrum and crustal reverberations, the attenuation mapped to the *PP* bounce point is relatively unaffected by these factors and we use this information to produce a map of lateral variations in compressional attenuation in the upper mantle.

2. Data and Processing

[6] We use the same data and processing steps as *Warren and Shearer* [2000] (hereinafter referred to as WS). We select our seismograms from the Incorporated Research Institutions for Seismology (IRIS) Fast Archive Recovery Method (FARM) database [*Ahern et al.*, 1995] for 1988 to 1999, which includes all earthquakes during this time with $M_W \geq 5.8$ (with $M_W \geq 5.5$ for quakes at $\geq$100 km depth). While the original database is composed of 20 Hz data, we have applied an antialiasing filter and resampled at 5 Hz for a local database that is used for a variety of seismic studies. We search the local database for all *P* arrivals at epicentral distances between 40° and 80° and all *PP* arrivals between 80° and 160° from shallow ($\leq$50 km depth) earthquakes. Next, after applying a Hanning taper we compute the spectrum for a 12.6-s-long signal window beginning 2 s before each predicted arrival time and for a 12.6-s-long noise window just preceding this. In the ensuing analysis we select spectra that have average signal-to-noise ratios of 2 or greater between 0.16 and 0.86 Hz.

3. Spectral Technique for Estimating Attenuation

[7] The computed spectrum, D^P for *P* waves and D^{PP} for *PP* waves, is determined by along-path attenuation *A*, near-source effects *S* (which include the source spectrum and near-source attenuation), near-receiver effects *R* (which include the known instrument response, the site response, and near-receiver attenuation), geometrical spreading *G*, and, for *PP* arrivals, the bounce point reflection coefficient *C*:

$$D^P(f) = A^P(f)\,S(f)\,R(f)/G$$
$$D^{PP}(f) = A^{PP}(f)\,S(f)\,R(f)C/G^2. \quad (1)$$

We correct each spectrum for the known instrument response, a high-frequency source spectral falloff of $\omega^{-2.15}$ (found by WS to be appropriate for this data set), and the globally averaged Q_α model of WS; thus, in the discussion that follows, D^P, D^{PP}, *S*, and *R* represent residual spectra with respect to this model. For the Q_α model we use the two-layer frequency-independent model with Q_α = 185 above 220 km depth and Q_α = 3250 below 220 km depth.

[8] The amplitude decay with frequency due to attenuation is

$$A(f) = A_0\ \exp[-\pi f\, t^*(f)], \quad (2)$$

where $t^* = \int dt/Q$. After taking the base 10 logarithm of each spectrum, we can estimate how attenuated the spectrum is from its slope. Since our measurements are of relative and not absolute amplitude we can disregard the frequency-independent terms (A_0, *G*, and *C*) which change the position but not the slope of the spectrum. When we measure the spectral slope we cannot compute t^* directly because it is frequency dependent. Rather, we first compute $\overline{t^*}$, which is t^* plus a frequency-dependent term:

$$\overline{t^*} = t^* + f\frac{dt^*}{df} = \frac{-1}{\pi}\left(\frac{d\ln A}{df}\right) \quad (3)$$

and then, after making assumptions about the form of the frequency dependence, translate $\overline{t^*}$ to t^*.

[9] The frequency dependence is generally modeled with an absorption band [e.g., *Liu et al.*, 1976], so there is a wide frequency band over which the frequency dependence is negligible. Both above and below this frequency band, the position of which is prescribed by upper and lower corner frequencies, there is a strong frequency dependence. The position of the absorption band is determined by properties such as pressure, temperature, and composition [*Lundquist and Cormier*, 1980], so it changes both laterally and with depth within the Earth. In WS we studied the average frequency dependence of attenuation and found that, in the upper mantle, the frequencies we are investigating are near the high-frequency end of the absorption band. However, as we will explain later, the size of the frequency-dependent term is very small in the upper mantle, so the $\delta\overline{t^*}$ values that we will present in this paper are roughly equivalent to δt^* values for the upper mantle.

4. Earthquake and Station Stacks

[10] In travel time seismology, station terms consisting of time offsets are commonly used to correct travel times when a given station routinely gives fast or slow times. We compute analogous terms for the attenuation measurements that indicate whether a station or earthquake routinely provides more or less attenuating spectra. To compute these terms we take advantage of our large quantity of data and the fact that most attenuation takes place at shallow depths. Since we have multiple sources for each receiver and multiple receivers for each source, we can approximate the attenuation beneath each source and receiver (denoted S_i for the *i*th earthquake and R_j for the *j*th station) by

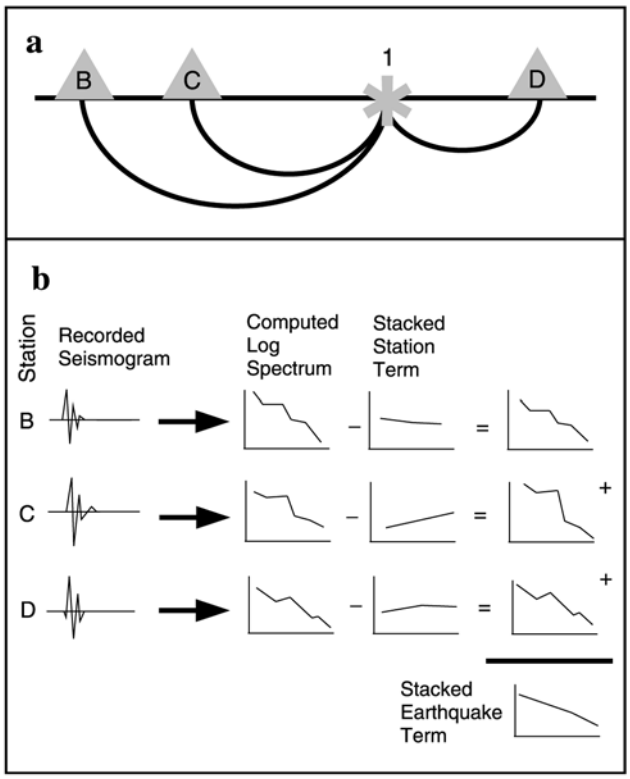

Figure 1. Cartoon explaining how we stack to obtain the earthquake terms. If earthquake 1 is recorded by stations B, C, and D (Figure 1a), we compute the earthquake term for earthquake 1 by stacking the log spectrum from earthquake 1 computed for stations B, C, and D after removing the station terms for stations B, C, and D (Figure 1b). In this case the earthquake stack for earthquake 1 can be expressed as $\log S_1 = (1/3)\sum_{j=B}^{D}[\log D_{1j}^P - \log R_j]$. An analogous procedure is used to compute the station terms.

stacking the appropriate P wave residual spectra, D_{ij}^P for the ith earthquake and jth station. We iteratively stack all log spectra recorded at each station after removing the appropriate earthquake stacks and all log spectra from each earthquake after removing the appropriate station stacks. For the ith earthquake, the earthquake stack is

$$\log(S_i) = \frac{1}{j}\sum_j \left[\log\left(D_{ij}^P\right) - \log\left(R_j\right)\right]. \quad (4)$$

For the jth station the station stack is

$$\log\left(R_j\right) = \frac{1}{i}\sum_i \left[\log\left(D_{ij}^P\right) - \log(S_i)\right]. \quad (5)$$

The stacking process is illustrated in Figure 1 for the earthquake stacks. This method maps all deviations from the average attenuation model to shallow depths beneath the stations and earthquakes. The resulting station terms include the near-receiver attenuation anomalies and the site response. The resulting earthquake terms include the near-source attenuation anomalies and deviations from the average source model. Since the two sets of terms are dependent upon each other we iterate the stacking process to find stable values.

[11] Requiring that each stack contain $\geq$10 spectra gives stacks for 142 stations and 876 earthquakes from 17,289 paths. If the stacks are dominated by the attenuation signal, we can measure the deviation from the average Q model from the shape of the stacked station and earthquake spectra. By fitting a straight line to the stacked log spectra between 0.16 and 0.86 Hz, as described in section 3, we measure $\delta\overline{t^*}$ relative to the 1-D attenuation model to compute the earthquake and station terms. Figure 2 shows the measured $\delta\overline{t^*}$ values for the earthquake and station stacks at their geographic locations and Figure 3 shows histograms of the measured $\delta\overline{t^*}$ values. Tables with the measured $\delta\overline{t^*}$ values are available in the electronic supplement[1]. Positive values indicate more attenuating than average regions, while negative values indicate less attenuating than average regions. The wider spread in values for the earthquake terms compared to the station terms probably reflects the additional complexities due to differences between source spectra and source depths. The zero mean values indicate that we have removed the average attenuation and source models.

[12] The patterns of positive and negative $\delta\overline{t^*}$ values seen in Figure 2 are relatively coherent over large areas. For example, both the station and earthquake terms tend to be negative across the Eurasian shield while positive earthquake terms are seen along the mid-ocean ridges, as would be expected based on their tectonic settings. An example not showing a correlation with tectonic setting is the station terms from islands in the Pacific, which tend to be large and positive. While these values do not correlate with the age of the ocean floor in these locations, they may reflect wave-propagation effects, such as focusing of energy or reverberations beneath the islands, that must be accounted for. In addition, there could be strong local attenuation beneath volcanic islands. The patterns in the earthquake terms in Figure 2b around the Pacific are blurred by the large numbers of earthquakes located there, but this area still shows coherent positive and negative values in the measurements, generally over smaller length scales than for the station terms. For both the earthquake and station terms, the large-scale patterns probably represent the effects of attenuation while the smaller variations probably reflect local crustal structures or differences in source spectra. The source terms may be further complicated by regional differences in source spectra.

[13] For two stations we have records from a pair of instruments at the same site for some of the time covered by our study, so we can look at the internal consistency of this method. When island station Raratonga (RAR) was installed, a surface sensor was installed in addition to the permanent borehole instrument to compare noise levels. Comparing our measured $\delta\overline{t^*}$ values for the surface seismometer with the borehole sensor shows a large difference in the two. The stack for the borehole instru-

[1]Supporting material is available via Web browser or via Anonymous FTP from ftp://ftp.agu.org, directory "apend" (Username = "anonymous", Password = "guest"); subdirectories in the ftp site are arranged by paper number. Information on searching and submitting electronic supplements is found at http://www.agu.org/pubs/esupp_about.html.

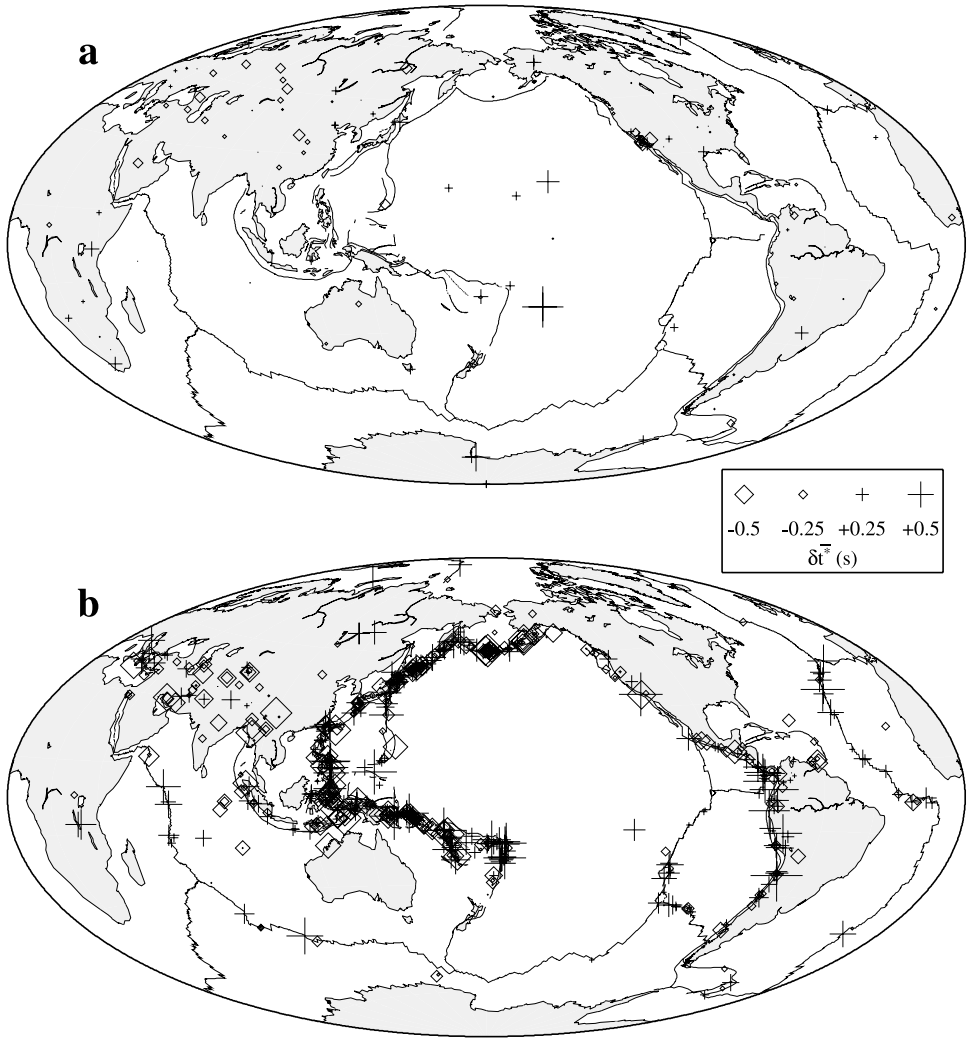

Figure 2. (a) Station and (b) earthquake $\delta\overline{t^*}$ measurements at their geographic locations.

ment (which averages 148 spectra) gives $\delta\overline{t^*}$ = 0.791 s while the surface sensor (which averages 33 spectra) gives $\delta\overline{t^*}$ = 0.550 s. The borehole instrument may have reduced amplitudes at higher frequencies in our passband due to the interference between the upgoing and downgoing pulses, although some of the difference could reflect the different earthquakes sampled. Both $\delta\overline{t^*}$ values suggest that the area is extremely attenuating, which would not be expected for ~100 Myr old oceanic crust. Of course the island is not representative of the surrounding oceanic crust and the high attenuation measurement probably reflects this.

[14] The South Pole station (SPA) has two channels available beginning in November 1998. Our measured $\delta\overline{t^*}$ value for the secondary channel over the limited time period (0.131 s from averaging 14 earthquake spectra) is similar to the value measured over the entire length of the study at the other instrument location (0.153 s from averaging 97 earthquake spectra). We can see that a given site gives a consistent response when the instrument is at a common location, as for station SPA. Thus, it is important to approximate the source and receiver effects by stacking the spectra, which also accounts for focusing/defocusing, source spectral differences, and instrument placement, rather than simply using the tectonic setting.

5. Lateral Variations in Attenuation at the *PP* Bounce Point

5.1. Mapping $\delta\overline{t^*}$

[15] While the station and earthquake terms provide a preview of the lateral variations in upper mantle attenuation, they also show that they can be biased by local crustal structures or source differences. We found the earthquake and station terms by stacking spectra from *P* waves, but the *PP* waves, which are at twice the range of the *P* waves, will be similarly affected since the two phases have the same takeoff angles, path lengths, and turning depths. Thus the *PP* waves will see the same structures beneath the earthquakes and stations as the *P* waves, and we correct the *PP* spectra (denoted D_{ij}^{PP} for the *i*th earthquake recorded at the *j*th station) for the appropriate earthquake and station terms to find attenuation at the *PP* bounce point:

$$\log(A_{ij}) = \log\left(D_{ij}^{PP}\right) - \log(S_i) - \log(R_j). \qquad (6)$$

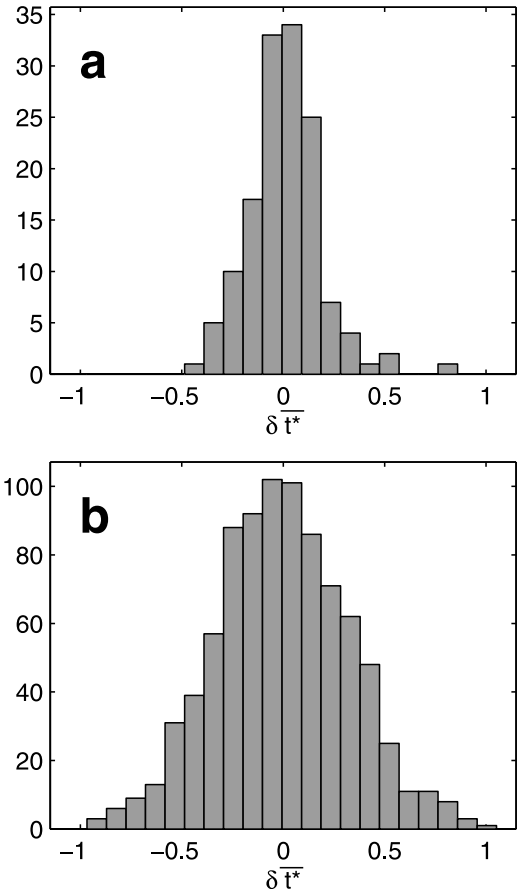

Figure 3. Histograms of the (a) station and (b) earthquake $\delta\overline{t^*}$ measurements.

Since lower mantle attenuation is small and we have corrected for the source- and receiver-side attenuation, the remaining spectrum should approximate attenuation near the *PP* bounce point in the upper mantle, as illustrated in Figure 4. There are 11,206 *PP* spectra with the appropriate earthquake and station stacks.

[16] As with the station and earthquake terms, we measure $\delta\overline{t^*}$ from the residual spectrum between 0.16 and 0.86 Hz. A histogram of these measurements is shown in Figure 5a. To reduce the scatter in the individual measurements and better elucidate the large-scale patterns of more and less attenuating regions, we compute average values for overlapping caps of 5° radius spaced by 5°, which divides the Earth into 1654 caps. The Fresnel zone for the *PP* bounce points is about 6° across, so the caps average over a larger area and have a greater smoothing effect. For caps with $\geq$5 measurements (76% of the caps), a histogram of the cap-averaged values is shown in Figure 5b and the geographic distribution of values is plotted in Figure 6a. There are up to 320 measurements per cap. We compute the standard errors for each cap with bootstrap resampling [*Efron*, 1982] of the $\delta\overline{t^*}$ measurements. A table containing the cap-averaged $\delta\overline{t^*}$ measurements, the number of measurements in each cap, and the standard errors is available in the electronic supplement. Caps of 2° radius spaced by 2° show similar patterns with more small-scale features, reflecting both actual structure and more noise.

[17] The *PP* bounce point $\delta\overline{t^*}$ values, like the earthquake and station terms, suggest that the amount of attenuation correlates with the tectonic setting. Indeed, when we bin the caps by tectonic region (following the regionalization of *Jordan* [1981], see Figure 6b) and compute the mean value for each type of region (see Figure 7) we see that the mean values follow a pattern consistent with that expected based on their tectonic history. The upper mantle beneath young

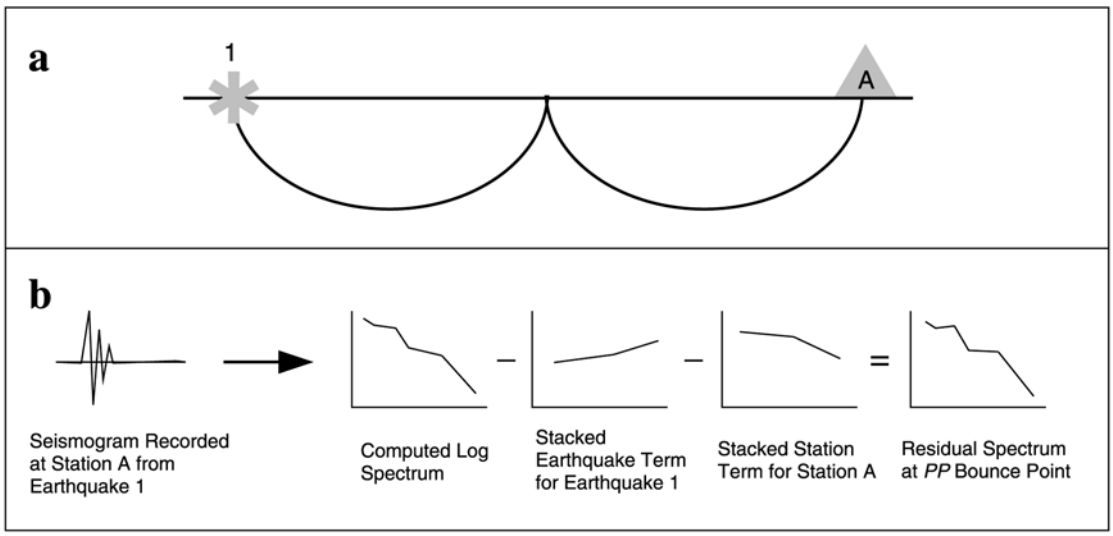

Figure 4. Cartoon explaining how we correct the *PP* spectra for the station and earthquake terms to determine attenuation at the *PP* bounce point. If earthquake 1 is recorded at station A as a *PP* wave (Figure 4a), we correct the computed log spectrum for the earthquake term from earthquake 1 and the station term from station A (Figure 4b). This can be expressed as $\log A_{1A} = \log D_{1A}^{PP} - \log S_1 - \log R_A$. Since most attenuation occurs in the upper mantle, the remaining spectrum should approximate attenuation in the upper mantle beneath the *PP* bounce point.

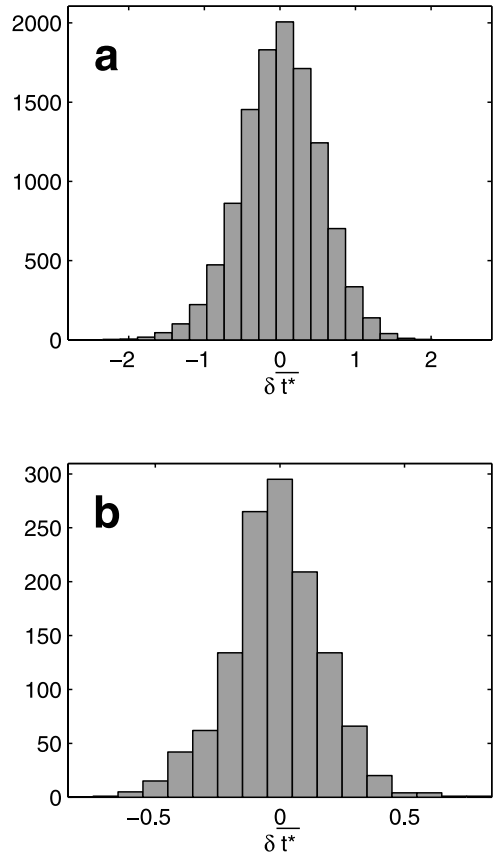

Figure 5. Histograms of (a) raw and (b) cap-averaged $\delta\overline{t^*}$ bounce point values for *PP* spectra, following corrections for near-source and near-receiver terms.

ocean floor (170 caps), where hot material is upwelling, is the most attenuating type of region, followed closely by intermediate-age oceans (429 caps). Old oceans (165 caps) are much less attenuating than young oceans. The least attenuating regions are the old continental shields and platforms (78 and 119 caps, respectively). Tectonically active zones (245 caps) are slightly more attenuating than old oceans. Subduction zones (52 caps) are about as attenuating as intermediate-age oceans.

5.2. Effect of Reverberations at the *PP* Bounce Point

[18] One potential source of bias is reverberations in the water column above oceanic *PP* bounce points. We test how large this effect is by creating a synthetic time series with delta functions at the expected arrival time of the *PP* wave and at the times of the first two water column reverberations (if they fall within the measured time window). The amplitude of the main pulse is set to 1 while the amplitudes of the reverberation arrivals are scaled to match their expected amplitudes based on reflection and transmission coefficients at the crust/water interface. Next, we compute the spectrum of this synthetic time series and measure $\overline{t^*}$ from the slope. For *PP* waves observed at 100° and 140°, the resulting $\overline{t^*}$ measurements for water depths of 2.5 to 7.0 km are plotted in Figure 8. For both distances the average $\overline{t^*}$ value over this depth range is 0.03 s, with the measured values as a function of water depth being random about this value. Except for a relatively small number of bounce points at water depths near 6 km, the expected bias is small and we make no corrections for water column reverberations. In any case, there is no observable correlation between our observed $\delta\overline{t^*}$ values and the small fraction of the oceans that are close to 6 km depth.

[19] For oceanic *PP* bounce points the effects of crustal reverberations will be similar to those seen in the water column. However, since the velocity contrast between the mantle and crust is not as sharp as the velocity contrast between the crust and water, the effect will not be as large. For continental *PP* bounce points the resulting *PP* spectrum will not be affected because the first reverberation (for crust $\geq$35 km thick) falls outside the time window.

5.3. Effect of Lower Mantle Attenuation Anomalies

[20] Lateral variations in Q at greater depths could also bias our measurements. However, the lower mantle contribution to t^* is small relative to the upper mantle contribution: based on the WS Q model and IASPEI travel times [*Kennett*, 1991], a *P* wave observed at 60° (or a *PP* wave at 120°) from a surface source spends 11% of its time in the top 220 km of the mantle while accumulating 68% of its t^*. For the *P* wave, the total t^* is 0.52 s, with 0.35 s contributed by the top 220 km of the mantle and the remaining 0.17 s from greater depths. To determine the effect of variations in attenuation in the lower mantle, we consider the effect of introducing a large attenuation anomaly to the lower mantle. If we make the entire path through the mantle below 220 km depth twice as attenuating as the globally averaged value (i.e., double Q^{-1}), the lower layer contribution to t^* increases to 0.33 s, an increase of 0.16 s. To get an increase in t^* of the same size from variations in Q^{-1} solely in the top 220 km of the mantle would require increasing Q^{-1} by a factor of 1.45, a significantly smaller percentage change in attenuation over a significantly shorter path length. Thus t^* is not very sensitive to variations in attenuation in the lower mantle, an area where large variations have not been observed [*Bhattacharyya*, 1996].

5.4. Variations in Q_α

[21] To convert the *PP* bounce point $\delta\overline{t^*}$ cap-averaged values to variations in Q_α, we need to make a few assumptions about the nature of attenuation in the Earth. First, we determine the depth range over which these variations are likely to occur. In WS the best fitting model had a thin highly attenuating layer atop the rest of the mantle, which had relatively large Q values. Modeling most of the attenuation to occur in the top few hundred kilometers of the mantle is consistent with the results of other studies [e.g., *Bhattacharyya et al.*, 1996], and we have constrained the variations to occur in the top 220 km. However, we do not have any depth resolution within this range and the thickness of the layer is somewhat arbitrary. If we had used a thicker layer the resulting Q^{-1} values and variations therein would be reduced in amplitude in comparison with what we present here. In addition, these values should be treated as average Q^{-1} values for this depth range since the thickness of the highly attenuating layer may vary around the globe.

[22] Next, since Q is related to t^* rather than the measured $\delta\overline{t^*}$, we consider the effect of the frequency dependent term in equation (3) so that we can relate these two

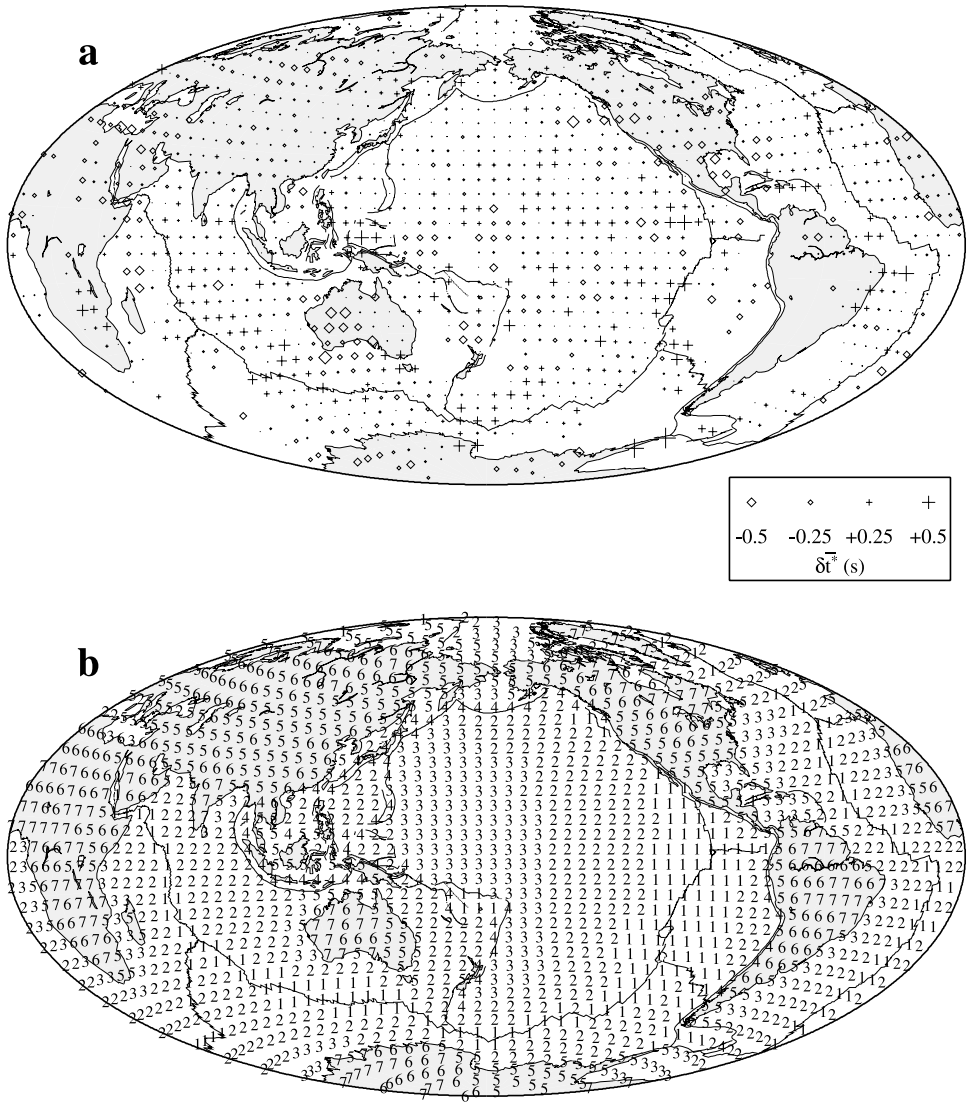

Figure 6. Map of cap-averaged $\delta\overline{t^*}$ values for caps with $\geq$5 measurements (Figure 6a) compared to the *Jordan* [1981] tectonic regionalization (Figure 6b), which is used in Figure 7. For the tectonic regions, 1 corresponds to young oceans, 2 corresponds to intermediate-age oceans, 3 corresponds to old oceans, 4 corresponds to subduction zones, 5 corresponds to tectonically active regions, 6 corresponds to platforms, and 7 corresponds to shields.

quantities. Both t^* and $\overline{t^*}$ can be written as the sums of their globally averaged values (t_0^* and $\overline{t_0^*}$, respectively) plus deviations from these averages (δt^* and $\delta\overline{t^*}$, respectively):

$$t^* = t_0^* + \delta t^* \tag{7a}$$

$$\overline{t^*} = \overline{t_0^*} + \delta\overline{t^*} \tag{7b}$$

Also note that for the average model we can write (3) as $\overline{t_0^*} = t_0^* + f(dt_0^*/df)$. Thus rearranging equation (3) and substituting these equations gives

$$\begin{aligned} t^* &= \overline{t^*} - f\frac{dt^*}{df} \\ &= \overline{t_0^*} + \delta\overline{t^*} - f\frac{d(t_0^* + \delta t^*)}{df} \\ &= t_0^* + f\frac{dt_0^*}{df} + \delta\overline{t^*} - f\frac{dt_0^*}{df} - f\frac{d(\delta t^*)}{df} \\ &= t_0^* + \delta\overline{t^*} - f\frac{d(\delta t^*)}{df}. \end{aligned} \tag{8}$$

To compute t_0^* for each cap, we use the 220-km-thick upper layer of the frequency-dependent model of WS at a frequency of 0.5 Hz (the midpoint for our frequency band) and the IASPEI 1991 velocity model. Since $\delta\overline{t^*}$ is what we have measured from each spectrum, the only unknown on the right side of the final equation is $f[d(\delta t^*)/df]$. Variations in this term would indicate that the position of the high-frequency end of the absorption band changes with location on Earth, perhaps reflecting differing temperatures or compositions. If we compare the values for t_0^* and $\overline{t_0^*}$ for the upper layer given in WS, we find that $(\overline{t_0^*} - t_0^*) = f(dt_0^*/$

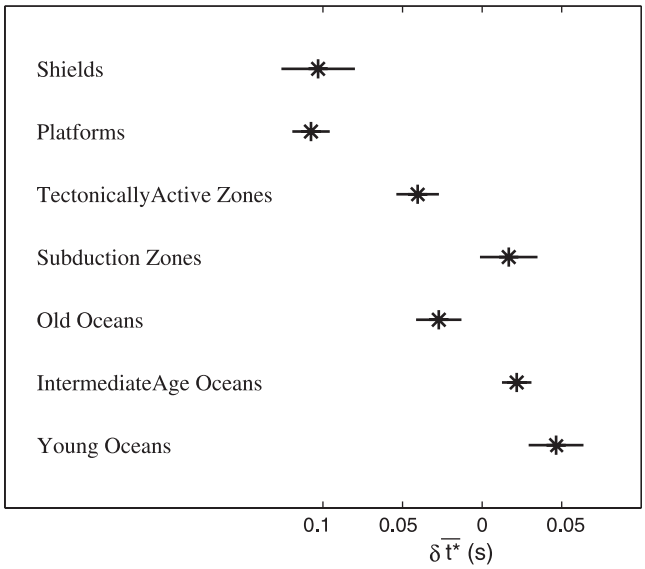

Figure 7. Cap-averaged $\delta\overline{t^*}$ values for *PP* spectra binned by the tectonic region of their bounce points.

df) = −0.05. Small deviations from the average model in absorption band position would result in $f[d(\delta t^*)/df]$ values closer to zero and we disregard it. Ignoring this term when it was significant would lead to underestimated t^* and Q^{-1} values. Assuming that $t^* = t_0^* + \delta\overline{t^*}$ allows us to compute Q^{-1} for each cap. The value used for t_0^* changes slightly between caps based on the average range of all rays bouncing within that cap.

[23] The Q^{-1} values and estimated errors for caps with ≥5 measurements are fit with spherical splines and plotted as a spherical harmonic expansion up to degree 12 in Figure 9. We can see that the shields across Eurasia and North America are less attenuating (blue) while more-attenuating regions (red) are found tracing the mid-ocean-ridge system and the mid-Pacific. There are exceptions to these patterns. For example, beneath southern Africa we see a more attenuating region and in the southwest Pacific we see a less attenuating region. We have blacked out areas with no data coverage.

6. Comparison of Earthquake Terms, Station Terms, and Bounce Point Measurements

[24] While the bias effects from water and crustal reverberations appear to be small, a comparison of the station terms, the earthquake terms, and the bounce point cap-averaged $\delta\overline{t^*}$ values shows that something in addition to attenuation must be influencing one, two, or all of them since there are areas where they disagree. It is not surprising that they are not in perfect agreement (in terms of both sign and magnitude of values) since they probably sample the earth in different ways. The earthquake and station terms inherently sample much smaller volumes than the bounce point measurements, which average over caps of 5° radius. They also cover different parts of the Earth. Below we compare regions that are sampled by more than one type of data.

[25] The ocean basins are almost exclusively covered by the bounce point measurements. There are isolated station terms on islands but, as discussed in section 4, they are not representative of the surrounding oceanic crust and are likely to be influenced by wave propagation effects. Not surprisingly, the only places they agree are in more attenuating parts of the ocean basins and we will not compare the oceanic station terms to the oceanic bounce point measurements or earthquake terms.

[26] There are earthquake terms along the mid-ocean ridges and subduction zones that we can compare with bounce point measurements in those areas. Along the Mid-Atlantic Ridge, the earthquake terms indicate that the spectra they represent contain less high frequency energy than the spectra for the average earthquake term. This suggests that the earthquakes themselves have fewer high frequencies and/or that the upper mantle beneath the earthquakes is more attenuating than average upper mantle. Based on the tectonic setting, we would expect a more attenuating region yet the bounce points measurements are not large. If a very highly attenuating region is concentrated right around the ridge axis, the bounce point averages may be reduced since they average over a much larger area.

[27] Along the East Pacific Rise there is good agreement between the earthquake terms and bounce point measurements where there are earthquakes. The magnitudes of the two types of measurements are about the same. Bounce point measurements along the Central Indian Ridge do not show additional attenuation along the ridge.

[28] The subduction zones around the western Pacific have many earthquakes and the corresponding earthquake terms are large in magnitude and of mixed sign. The bounce point measurements are very small in magnitude. Since the bounce point measurements average over a 5°-radius cap, large variations, such as those seen in the neighboring positive and negative earthquake terms, would be smoothed out.

[29] Since continents have better station coverage than the oceans, the continents provide more places to compare the different types of data. All three types of data can be used to estimate attenuation beneath Eurasia, although the geographical coverage of each type varies, and all of them, as evidenced by negative values, support most of the

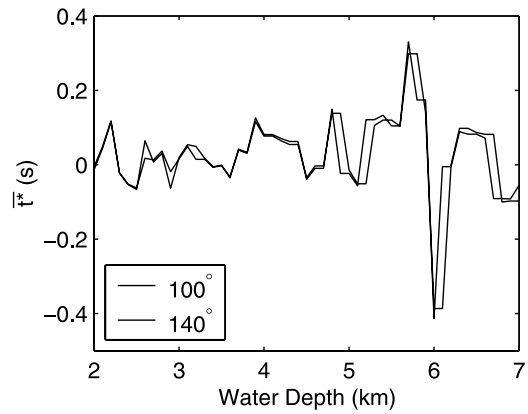

Figure 8. Effect of reverberations in water column above the *PP* bounce point. For water depths between 2.5 and 7.0 km the expected bias to $\overline{t^*}$ measurements for *PP* waves observed at 100° and 140° is small except for water depths near 6 km.

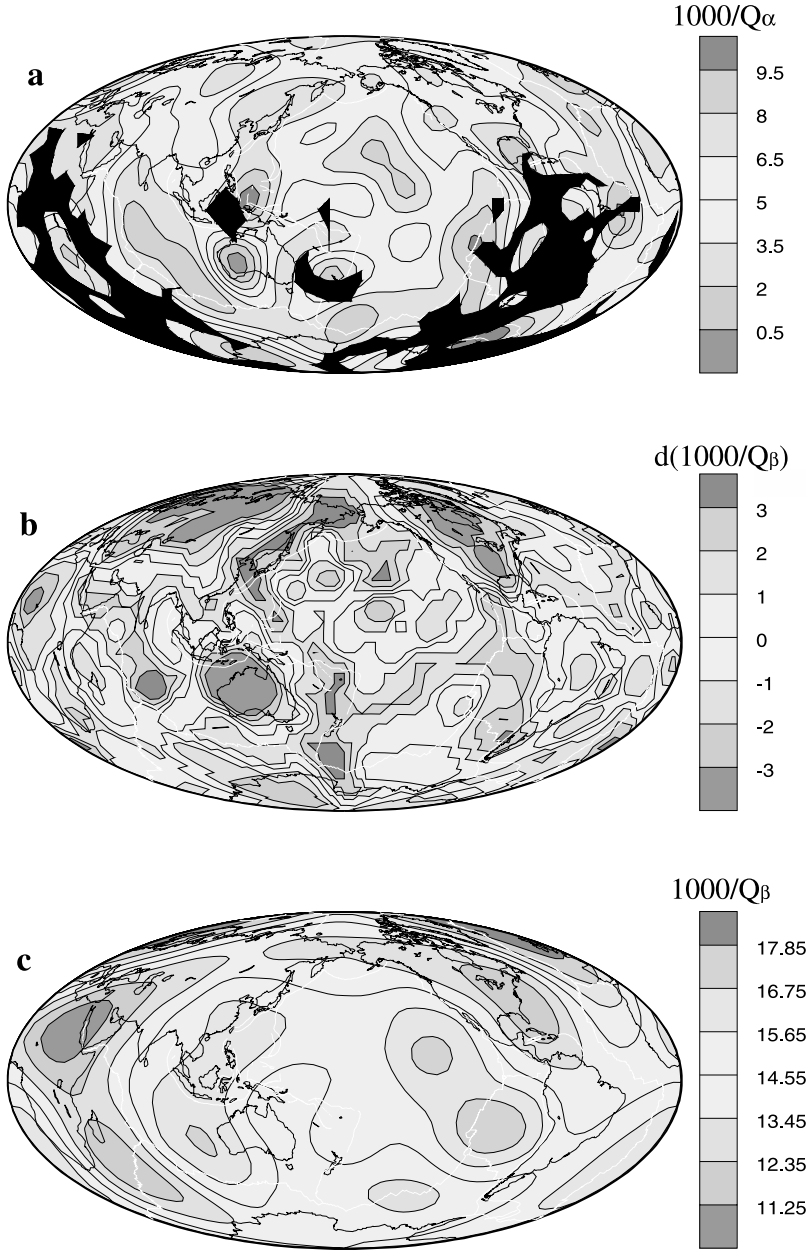

Figure 9. (a) Map of 1000/Q for the top 220 km of the mantle. Black areas indicate regions with no data. The (b) *Selby and Woodhouse* [2000] and (c) *Romanowicz* [1995] models are shown for comparison. For the Selby and Woodhouse model, variations from average 1000/Q_β are mapped, while the actual 1000/Q_β values are mapped for the Romanowicz model. See color version of this figure at back of this issue.

continent overlying a less-attenuating-than-average upper mantle. The station terms, which are concentrated in the northern part of the continent, are very consistently negative. The bounce point measurements are also consistently negative and of approximately the same magnitude. The earthquake terms, which are mainly to the south of the station terms, are mostly negative but not as consistently as the station terms and bounce point measurements. The upper mantle beneath the eastern part of the continent is more attenuating: we find positive station terms, earthquake terms, and bounce point measurements there.

[30] Antarctica has positive station terms that correlate with more attenuating bounce point measurements. The negative earthquake terms are close to near-zero attenuation anomalies.

[31] Within Africa, the earthquake terms, station terms, and bounce point measurements tend to cover different, although neighboring, regions and appear to be consistent. The coverage in southern Africa overlaps a little more than in other places and positive values are found. Bounce point measurements on and near the Arabian Peninsula are less attenuating than average. The lone station term on the Arabian Peninsula is also negative.

[32] Australia is mostly covered by bounce point measurements. The few station and earthquake terms on the continent agree in sign with the bounce point measurements.

[33] Since the different types of data cover different parts of the Earth and sample it in different ways, we cannot make a quantitative assessment of how similar the resulting patterns of more and less attenuating areas are. On a qualitative basis we can see that there is good agreement between the different types of data as regions of common coverage tend to have the same sign and neighboring regions also tend to show continuity. Areas of disagreement can often be attributed to specific factors such as differences in how the different types of data sample or average areas or systematic differences in source spectra between regions.

7. Comparison With Previous Studies

[34] We compare our Q_α model with the surface wave Q models of *Selby and Woodhouse* [2000] and *Romanowicz* [1995] in Figure 9. Selby and Woodhouse present degree-20 maps of attenuation constructed from Rayleigh waves at periods of 73 s, which we plot here, and 146 s. Model QR19 [*Romanowicz*, 1995], which is constructed from Rayleigh waves, is a 10° block model at periods of 100–300 s. The model is equivalent to degree 6 or 7, so it does not show the smaller-scale features that the other models do. We plot the average value for the top 220 km, which is equivalent to the depth range of our model.

[35] The mean Q_α of our model is 2.9 times larger than the mean Q_β value of QR19. For a Poisson solid with infinite Q_κ we would expect a ratio of 2.25, so the observed ratio is a little larger than what we would expect. This may be caused by the different frequency bands of the measurements. The Q_β measurements are likely to be within the flat portion of the absorption band while the higher frequency Q_α measurements may be in a band where the Q^{-1} amplitudes are decreasing. This would lead to larger values for Q_α and therefore Q_α/Q_β. The mean value for the Selby and Woodhouse model is the PREM value [*Dziewonski and Anderson*, 1981], which is approximately the same as QR19. The lateral variations in our model are larger than the lateral variations in the surface wave models in both absolute magnitude and percent variations, although this could simply be a result of different damping parameters and spatial averaging for the different data sets.

[36] Given the different types of data (body waves versus surface waves), types of attenuation mapped (compressional versus shear), and frequency contents, it would not be surprising if the resulting maps had substantial differences between them. Yet the large-scale patterns of more and less attenuating regions are remarkably similar. All the models show that Eurasia and North America tend to be less attenuating while the Pacific tends to be more attenuating.

[37] These patterns are generally consistent with what we would expect based on the tectonic history of these regions. We can see this more clearly by looking at specific regions. Both our model and the Selby and Woodhouse model show the same pattern for Australia. The continent progresses from more attenuating in the east to less attenuating in the west. This pattern reflects the geologic history of the continent and is also seen in tomographic images of the velocity structure [*Simons et al.*, 1999]. Western Australia, the least attenuating part of the continent, is composed of Archean crust and has fast velocities. More attenuating eastern Australia is composed of younger Phanerozoic crust, and slower velocities are observed there. Central Australia is intermediate in age, amount of attenuation, and wave speeds.

[38] There are some regions that are quite interesting because they do not follow what we would expect based on their tectonic history. For example, beneath southern Africa we see a more attenuating region while, based on its tectonic setting (i.e., cratons), we would expect a less attenuating region. This area has anomalously high topography and there has been some controversy about what is causing this. *Lithgow-Bertelloni and Silver* [1998] suggested that the high topography is supported by anomalies in the lower mantle. However, the high attenuation we see would suggest high temperatures in the upper mantle. Recent velocity models [*Zhao et al.*, 1999; *Priestley*, 1999; *James et al.*, 2001] suggest that the top ~120 km of the mantle has fast velocities, but that it may be underlain by a low-velocity zone or at least a region with slower than globally averaged velocities, which may indicate elevated temperatures in the region. There are isolated regions, such as the Bushveld complex which was intruded during the Proterozoic era, with lower velocities [*James et al.*, 2001], but they do not cover large enough areas to be responsible for the signal we see. While heat flow measurements in southern Africa do not suggest elevated upper mantle temperatures [*Jones*, 1988], the high attenuation does appear to be a robust result as it is also seen in the Selby and Woodhouse model. Since our model is at a much lower resolution than the regional velocity models, we cannot resolve the detailed structures seen in the velocity models and identify them with specific geologic features.

[39] Our model does not correctly predict some specific regions of known attenuation. For example, the tectonically active western United States should be a more attenuating region. We would also expect a much stronger contrast between the North American continent and the eastern Pacific Ocean, as is seen in global tomographic models of the velocity structure. However, the broad agreement between the global attenuation models suggests that this is a resolution problem, not a defect of the method. Only large scale attenuation differences can be seen with this method since we average over relatively large areas.

8. Conclusions and Future Work

[40] In this paper we have presented a new method for mapping attenuation and applied it to relatively high-frequency compressional waves. We compute spectra from *P* and *PP* arrivals and, assuming that most attenuation and variations therein occur at shallow depths, map the attenuation anomalies to the regions around the earthquakes, stations, and bounce points. With this method we produce the first global map of the lateral variations in compressional attenuation in the upper mantle at periods between 0.16 and 0.86 Hz.

[41] The resultant patterns of more and less attenuating regions show general agreement with tectonic features: the upper mantle beneath continents tends to be less attenuating while the upper mantle beneath the ocean basins tends to be more attenuating. While there are some regions where our map does not agree with known attenuation, there are many

areas, such as Australia, the Eurasian shield, and the East Pacific Rise, where our model does correctly predict attenuation. The large-scale features are also similar to surface wave maps of shear wave attenuation.

[42] In the future we will look more closely at the relationship between compressional and shear attenuation. It is important to determine if the differences we see between models are due to the methods used or intrinsic differences in the attenuation of compressional and shear waves. Data from different frequency bands will help us constrain the frequency dependence of attenuation, which in turn will tell us about the thermal and compositional states of the mantle.

[43] **Acknowledgments.** We thank Paul Earle and Luciana Astiz for help obtaining the FARM data and IRIS for providing and maintaining the database. Neil Selby and Barbara Romanowicz kindly provided their attenuation models. This work was supported by an NSF Graduate Research Fellowship and NSF grants EAR96-14350 and EAR99-09267. We thank Associate Editor Ed Garnero, Jeroen Ritsema, and an anonymous reviewer for constructive reviews.

References

Ahern, T., R. Benson, and K. Creager, New FARM products, yours for the picking, *IRIS Newsl.*, *14*, 14–15, 1995.

Bhattacharyya, J., Three-dimensional anelastic structure of Earth, Ph.D. thesis, Univ. of Calif., San Diego, La Jolla, 1996.

Bhattacharyya, J., G. Masters, and P. Shearer, Global lateral variations of shear wave attenuation in the upper mantle, *J. Geophys. Res.*, *101*, 22,273–22,289, 1996.

Billien, M., J.-J. Lévêque, and J. Trampert, Global maps of Rayleigh wave attenuation for periods between 40 and 150 seconds, *Geophys. Res. Lett.*, *27*, 3619–3622, 2000.

Der, Z. A., W. D. Rivers, T. W. McElfresh, A. O'Donnell, P. J. Klouda, and M. E. Marshall, Worldwide variations in the attenuative properties of the upper mantle as determined from spectral studies of short-period body waves, *Phys. Earth Planet. Inter.*, *30*, 12–25, 1982.

Der, Z. A., A. C. Lees, V. F. Cormier, and L. M. Anderson, Frequency dependence of Q in the mantle underlying the shield areas of Eurasia, part I, Analyses of short and intermediate period data, *Geophys. J. R. Astron. Soc.*, *87*, 1057–1084, 1986.

Ding, X.-Y., and S. P. Grand, Upper mantle Q structure beneath the East Pacific Rise, *J. Geophys. Res.*, *98*, 1973–1985, 1993.

Durek, J. J., and G. Ekström, A radial model of anelasticity consistent with long-period surface-wave attenuation, *Bull. Seismol. Soc. Am.*, *86*, 144–158, 1996.

Dziewonski, A. M., and D. L. Anderson, Preliminary reference Earth model (PREM), *Phys. Earth Planet. Inter.*, *25*, 297–365, 1981.

Efron, B., *The Jackknife, the Bootstrap and Other Resampling Plans*, *CBMS-NSF Reg. Conf. Ser. Appl. Math.*, vol. 38, Soc. for Ind. and Appl. Math., Philadelphia, Pa., 1982.

Flanagan, M. P., and D. A. Wiens, Attenuation structure beneath the Lau back arc spreading center from teleseismic *S* phases, *Geophys. Res. Lett.*, *17*, 2117–2120, 1990.

Grand, S. P., R. D. van der Hilst, and S. Widiyantoro, Global seismic tomography: A snapshot of convection in the Earth, *GSA Today*, *7*, 1–7, 1997.

James, D. E., M. J. Fouch, J. C. VanDecar, S. van der Lee, and Kaapvaal Seismic Group, Tectospheric structure beneath southern Africa, *Geophys. Res. Lett.*, *28*, 2485–2488, 2001.

Jones, M. Q. W., Heat flow in the Witwatersrand Basin and environs and its significance for the South African shield geotherm and lithosphere thickness, *J. Geophys. Res.*, *93*, 3243–3260, 1988.

Jordan, T. H., Global tectonic regionalization for seismological data analysis, *Bull. Seismol. Soc. Am.*, *71*, 1131–1141, 1981.

Kennett, B. L. N., *IASPEI 1991 Seismological Tables*, Res. Sch. of Earth Sci., Aust. Natl. Univ., Canberra, ACT, 1991.

Lithgow-Bertelloni, C., and P. Silver, Dynamic topography, plate driving forces, and the African superswell, *Nature*, *395*, 269–273, 1998.

Liu, H.-P., D. L. Anderson, and H. Kanamori, Velocity dispersion due to anelasticity: Implications for seismology and mantle composition, *Geophys. J. R. Astron. Soc.*, *47*, 41–58, 1976.

Lundquist, G. M., and V. F. Cormier, Constraints on the absorption band model of Q, *J. Geophys. Res.*, *85*, 5244–5256, 1980.

Masters, G., S. Johnson, G. Laske, and H. Bolton, A shear-velocity model of the mantle, *Philos. Trans. R. Soc. London, Ser. A*, *354*, 1385–1410, 1996.

Mitchell, B. J., Anelastic structure and evolution of the continental crust and upper mantle from seismic surface wave attenuation, *Rev. Geophys.*, *33*, 441–462, 1995.

Priestley, K., Velocity structure of the continental upper mantle: Evidence from southern Africa, *Lithos*, *48*, 45–56, 1999.

Romanowicz, B., A global tomographic model of shear attenuation in the upper mantle, *J. Geophys. Res.*, *100*, 12,375–12,394, 1995.

Selby, N. D., and J. H. Woodhouse, Controls on Rayleigh wave amplitudes: Attenuation and focusing, *Geophys. J. Int.*, *142*, 933–940, 2000.

Sheehan, A. F., and S. C. Solomon, Differential shear wave attenuation and its lateral variation in the North Atlantic region, *J. Geophys. Res.*, *97*, 15,339–15,350, 1992.

Simons, F. J., A. Zielhuis, and R. D. van der Hilst, The deep structure of the Australian continent from surface wave tomography, *Lithos*, *48*, 17–43, 1999.

van der Hilst, R. D., S. Widiyantoro, and E. R. Engdahl, Evidence for deep mantle circulation from global tomography, *Nature*, *386*, 578–584, 1997.

Warren, L. M., and P. M. Shearer, Investigating the frequency dependence of mantle Q by stacking P and PP spectra, *J. Geophys. Res.*, *105*, 25,391–25,402, 2000.

Widmer, R., G. Masters, and F. Gilbert, Spherically symmetric attenuation within the Earth from normal mode data, *Geophys. J. Int.*, *96*, 541–553, 1991.

Zhao, M., C. A. Langston, A. A. Nyblade, and T. J. Owens, Upper mantle velocity structure beneath southern Africa from modeling regional seismic data, *J. Geophys. Res.*, *104*, 4783–4794, 1999.

P. M. Shearer and L. M. Warren, IGPP, Scripps Institution of Oceanography, University of California, San Diego, La Jolla, CA 92093-0225, USA. (lwarren@ucsd.edu)

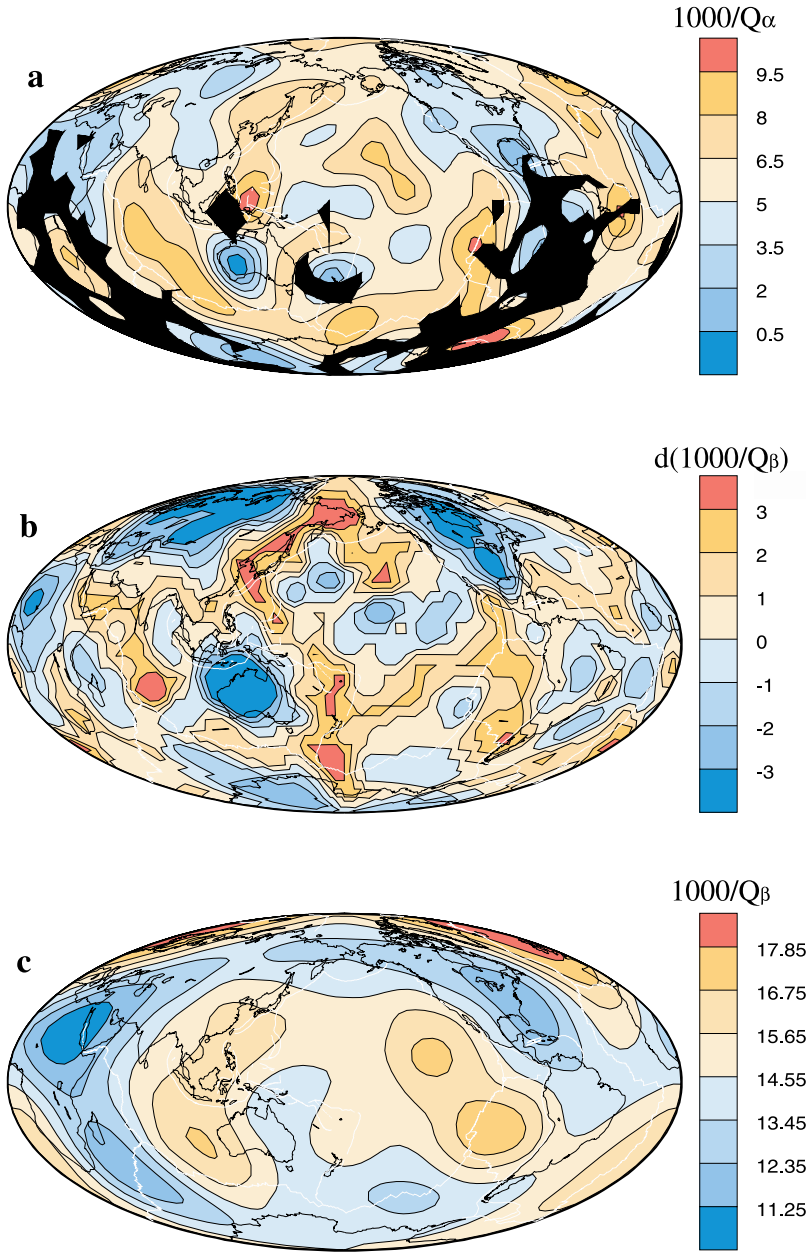

Figure 9. (a) Map of 1000/Q for the top 220 km of the mantle. Black areas indicate regions with no data. The (b) *Selby and Woodhouse* [2000] and (c) *Romanowicz* [1995] models are shown for comparison. For the Selby and Woodhouse model, variations from average 1000/Q_β are mapped, while the actual 1000/Q_β values are mapped for the Romanowicz model.